J. Fluid Mech. (2010), *vol.* 656, *pp.* 458–480.
doi:10.1017/S0022112010001230

Linear and nonlinear spatio-temporal instability in laminar two-layer flows

P. VALLURI†, L. Ó NÁRAIGH‡, H. DING¶ AND P. D. M. SPELT‖

Department of Chemical Engineering, Imperial College London SW7 2AZ, UK

(Received 9 May 2009; revised 8 March 2010; accepted 8 March 2010; first published online 21 May 2010)

The linear and nonlinear spatio-temporal stability of an interface separating two Newtonian fluids in pressure-driven channel flow at moderate Reynolds numbers is analysed both theoretically and numerically. A linear, Orr–Sommerfeld-type analysis shows that most of such systems are unstable. The transition to an absolutely unstable regime is investigated, and is shown to occur in an intermediate range of Reynolds numbers and ratios of the thicknesses of the two layers, for near-density matched fluids with a viscosity contrast. A critical Reynolds number is found for transition from convective to absolute instability of relatively thin films. Results obtained from direct numerical simulations (DNSs) of the Navier–Stokes equations for long channels using a diffuse-interface method elucidate that waves generated by random noise at the inlet show that, near the inlet, waves are formed and amplified strongly, leading to ligament formation. Successive waves coalesce with each other further downstream, resulting in longer larger-amplitude waves further downstream. In the linearly absolute regime, the characteristics of the spatially growing wave near the inlet agree with that of the saddle point as predicted by the linear theory. The transition point from a convective to an absolute regime predicted by linear theory is also in agreement with a sharp change in the value of a healing length obtained from the DNSs.

1. Introduction

This study of spatio-temporal stability of two-layer channel flows is motivated by the practical problem of removal of viscous soils in industrial plant during cleaning and product turnover operations. Standard practice is to displace the more viscous product fluid (which initially fills entire pipelines) by water, resulting in viscous films being left behind on pipe walls by a finger of water. These films are found by our test simulations for laminar flows (to be reported elsewhere) to be typically around 0.3 pipe radius thick, and to be sheared by the continued water flow. The resulting film displacement is anticipated to be strongly affected by the evolution of waves on the film surface. Also, most of the previous work on shear-induced interfacial wave evolution considers the linear temporal stability problem whereas the spatio-temporal

† Present address: School of Engineering, The University of Edinburgh, Kings Buildings, Edinburgh EH9 3JL, UK

‡ Present address: School of Mathematical Sciences, University College Dublin, Belfield, Dublin 4, Ireland

¶ Present address: Department of Chemical Engineering, University of California, Santa Barbara,CA 93106-5080, USA

‖ Email address for correspondence: p.spelt@imperial.ac.uk

problem has not yet received much attention. We review this literature very briefly here, along with spatio-temporal studies of related systems. The present study has two main objectives: to further extend previous studies of the linear problem (especially to include relatively thin films), and to undertake the direct numerical simulation (DNS) of open systems (i.e. with an inlet). The significant issue here is the comparison between the results obtained from these approaches, which hitherto has been addressed primarily for nonlinear temporal growth.

Of the main mechanisms that may lead to linear temporal growth, the one due to a viscosity stratification (Yih 1967) is usually dominant for a two-layer flow of different fluids. Viscosity stratification leads to net work being done by the perturbation velocity and stress at the interface. Boomkamp & Miesen (1996) verified that this mechanism plays an important role in many papers on interfacial instability, by using an energy budget. Other mechanisms for instability are also conveniently summarized by Boomkamp & Miesen (1996). Of particular importance for laminar two-layer flow is a Tollmien–Schlichting or shear-type mechanism (possibly in both fluids). Although the Yih mechanism usually dominates, its growth rate being rather large and shear modes only being unstable beyond a critical Reynolds number with relatively low growth rates, competition between these modes has been observed by particular choices of flow parameters (Yecko, Zaleski & Fullana 2002). The specific problem of the stability of two-layer channel flow has been studied in detail by Yiantsios & Higgins (1988); detailed findings of an energy budget can be found in Sahu *et al.* (2007).

Practical systems are of finite size, however, and the linear spatio-temporal growth of disturbances (possibly introduced at an inlet) may be rather different from that predicted by a temporal linear analysis. Reviews of the analysis of spatially evolving systems can be found in Huerre & Monkewitz (1990) and Chomaz (2005). Most previous work in this field is on single-phase flows, but it includes free-surface flows such as falling films down a fibre (Duprat *et al.* 2007), and miscible three-layer systems (Sahu *et al.* 2009).

In § 3 we perform a spatio-temporal linear stability analysis for two-dimensional two-layer immiscible channel flows. Apart from investigating the nature of spatio-temporal instability in these systems, a further objective is to provide the benchmark data necessary in subsequent sections on DNSs. A full parametric study of the linear analysis turns out to be not necessary, as the results are qualitatively similar to those reported recently in Sahu *et al.* (2009) for miscible three-layer systems. An issue not resolved by Sahu *et al.* (2009), however, is the behaviour of relatively thin films, due to limitations of their numerical method. Our results indicate that this is rather important, so in § 3 we focus primarily on the dependency of the results on the ratio of the interfacial height to the channel height including the thin film regime. Also, the present numerical method allows us to investigate in detail the various spatial branches, and the coalescence of some of these into a saddle point.

The main objective of this paper is the DNS of the nonlinear behaviour of two-dimensional two-layer channel flows, and to aim to compare with the linear theory of § 3. Most previous work in this field is for the nonlinear temporal evolution, i.e. on the DNS of two-layer flows subject to streamwise-periodic boundary conditions, which usually leads to ligament formation (e.g. Boeck *et al.* 2007). We briefly revisit this problem in § 4.2, both as a numerical (convergence) test, and to further investigate how and at what rate ligaments are extended. Ligaments are observed in subsequent sections in larger-scale flows.

In the main problem studied here (§ 4.4), the periodic conditions are dropped, and a two-layer flow through a channel of finite length is simulated. Previous work in

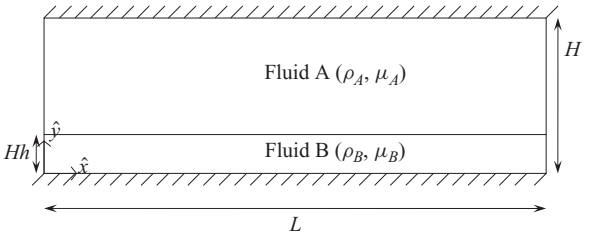

FIGURE 1. Schematic illustration of the flow geometry.

this area is limited essentially to the very recent study by Fuster *et al.* (2009), on the DNS of jet atomization. The present paper attempts to compare against the full spatio-temporal analysis, rather than a comparison against a temporal analysis, which was done by Fuster *et al.* (2009). Also, tests by us show that great care must be taken with the implementation of the inlet conditions. We introduce random noise at the channel inlet, akin to the methodology proposed previously by Chang, Demekhin & Kalaidin (1996) for thin falling films, which appears not to have been done previously.

The numerical method used here is that of Ding, Spelt & Shu (2007), which is a diffuse-interface method to track interfaces in conjunction with a projection method to solve the equations of motion for two-phase incompressible fluids. This method has been used and tested against previous work by others (who used a different numerical method) in Ding *et al.* (2007) and in several other papers, including Ding & Spelt (2008). The present problem poses several challenges. In order to compare with linear theory, the simulations must be highly resolved whilst relatively long domains must be simulated. A further concern is the use of such a diffuse-interface method, which necessarily smears the discrete jump in fluid properties across the interface over an interfacial region of finite thickness, which might affect the linear growth regime resulting from the simulations. Conveniently, however, the thickness of the interfacial region is well controlled by an input parameter of the diffuse-interface method, and we shall choose this to be proportional to the grid spacing. Both of these concerns are therefore important matters of convergence with respect to the grid spacing. We present evidence of convergence for the problem at hand at various stages in this paper.

2. Problem formulation

We consider immiscible two-phase flow in a rectangular horizontal channel of dimensional height H and dimensional length L, as depicted in figure 1; both the phases are considered Newtonian and incompressible. The upper fluid has viscosity μ_A and density ρ_A; the lower fluid has viscosity μ_B and density ρ_B. The streamwise and wall-normal directions are parallel to $\hat{x}$ and $\hat{y}$, respectively, as indicated in figure 1. The flow is driven by a pressure gradient along the $\hat{x}$ direction and is bounded by walls at $\hat{y}=0$ and $\hat{y}=H$, respectively. We shall consider systems with periodic boundary conditions as well as open systems with an inlet at $\hat{x}=0$ and an outlet at $\hat{x}=\hat{L}$. The dimensional location of the interface is at $\hat{y}=\hat{h}+\hat{\eta}(\hat{x},\hat{t})$, where $\hat{h}$ and $\hat{\eta}$ correspond to the unperturbed interfacial position and the amplitude of an applied disturbance, respectively. We introduce the following dimensionless variables (without carets),

$$\hat{\boldsymbol{x}} = H\boldsymbol{x},\ \hat{h} = Hh,\ \hat{\eta} = H\eta,\ \hat{\boldsymbol{u}} = V\boldsymbol{u},\ \hat{p}_i = -\rho_i g(\hat{y}-\hat{h}) + \frac{\mu_A V}{H}p, \hat{t} = (H/V)t, \quad (2.1)$$

where $\boldsymbol{u}=(u,v)$ and p are velocity and pressure, respectively. The velocity scale is chosen to be $V=Q/H$, where Q is the total volumetric flow rate through the

channel. These scalings result in the following main dimensionless parameters,

$$Re = \frac{\rho_A V H}{\mu_A}, \quad m = \frac{\mu_B}{\mu_A}, \quad r = \frac{\rho_B}{\rho_A}, \quad \Gamma = \frac{\gamma}{\mu_A V}, \quad G = \frac{(\rho_B - \rho_A) g H^2}{\mu_A V}. \tag{2.2}$$

Here, Re is a Reynolds number, m and r represent viscosity and density ratios, respectively, Γ is an inverse capillary number and G is a Bond number (a Weber number would correspond to $We = Re/\Gamma$). In the following, two approaches are followed to solve the equations of motion, a linear Orr–Sommerfeld-type analysis and a DNS. Further details of the method of solution are provided in these sections, including the dimensionless equations of motion in § 4.1).

3. Linear spatio-temporal stability analysis

Denoting a small-amplitude disturbance to the flat interface by $\eta = \epsilon\tilde{\eta} e^{i(\alpha x - \omega t)}$, the wavenumber is complex in this spatio-temporal analysis, $\alpha = \alpha_r + i\alpha_i$, and the complex frequency is denoted by $\omega = \omega_r + i\omega_i$. We use here the problem formulation as stated in Sahu *et al.* (2007) (but for Newtonian fluids) in terms of the perturbation in the streamfunction $\epsilon\psi(y)e^{i(\alpha x - \omega t)}$, obtained after linearization of the governing equations (presented in the Appendix) with respect to ϵ. This results in an eigenvalue problem, with as unknowns the eigenfunction $\psi(y)$ and a dispersion relation between α and ω. This problem is solved here using a spectral collocation method at a specified order of the Chebyshev polynomials in each of the two fluid layers. For all cases considered, 51 collocation points in the upper layer and from 15 (for $h \leqslant 0.05$) to a maximum of 51 (for $h = 0.5$) in the lower layer were sufficient to achieve convergence. The present implementation of the numerical method does not require an equal number of collocation points to be used in both layers (as was the case in Sahu *et al.* 2007, 2009), thereby allowing us to investigate a large range of values for the depth ratio h. Furthermore, the use of a specialized eigenvalue solver (Trefethen 2000) (details can be found in the Appendix) obviates the need for any explicit operations to remove the infinite eigenvalues from the problem, or to rebalance the problem to take account of ill-conditioning, difficulties which Boomkamp *et al.* (1997) encountered in their work. We have verified that the results from this entirely new code used here agrees with those of Sahu *et al.* (2007) and, when using a turbulent base state, with the results of Miesen & Boersma (1995).

We follow here the notation of, for example, Huerre & Monkewitz (1990). The flow is said to be linearly unstable if the most dangerous mode in the temporal analysis is unstable. Unstable parallel flows are classified as convectively unstable if initially localized pulses are amplified in at least one moving frame of reference but are damped in a laboratory frame, and absolutely unstable if such pulses lead to growing disturbances in the entire domain in a laboratory frame. The distinction is especially important in the determination of global stability of non-parallel systems (e.g. Chomaz 2005). An unstable parallel flow is absolutely unstable if the following criteria have all been met: (i) if $\omega_{i0} \equiv \omega_i(\alpha_0) > 0$, where α_0 is the wavenumber at which the group velocity $c_g = \partial\omega/\partial\alpha$ is zero, (ii) if the corresponding saddle point α_0 in the complex α plane is the result of the coalescence of spatial branches that originate from opposite half-planes at higher and positive ω_i and (iii) the saddle point pinches at ω_{i0}; this is verified by locating a cusp at ω_{i0} in the complex ω plane (Lingwood 1997; Schmid & Henningson 2000) and ensuring that the complex wavenumber corresponding to the pinching point coincides with α_0. Other unstable

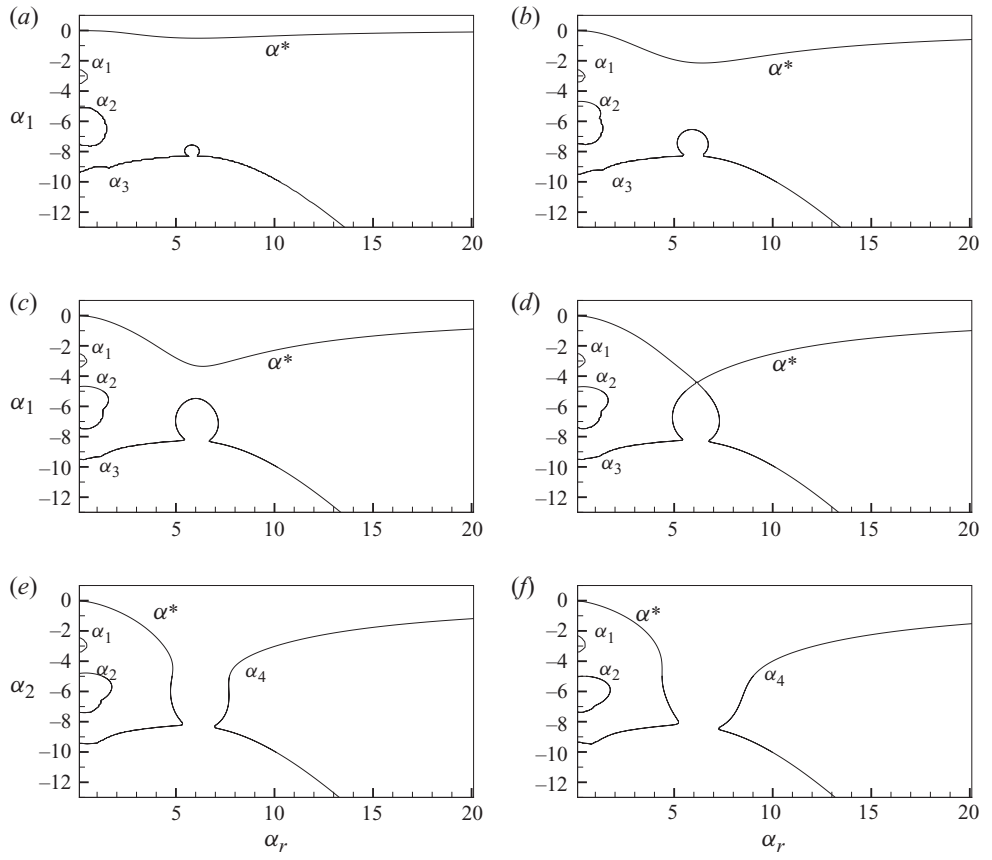

FIGURE 2. Spatial branches (at $\omega_i = 0$) for the system defined by $h = 0.3$, $m = 30$, $r = 1$, $\Gamma = 0.01$ and $G = 0$ at various Re ($Re = 5$, 30, 49, 55, 70, 100 in (a), (b), (c), (d), (e), (f), respectively). Transition from convective to absolute behaviour occurs at $Re = 55$.

flows are convectively unstable. Example results are shown and discussed further below (figure 4).

We have solved the Orr–Sommerfeld-type problem for $(\alpha_r, \alpha_i) = [(0.1, 120) \times (50, -120)]$. We have done this for $m = 10, 20, 30, 100, 1000$, $r = 1, 1.3, 100$, and combinations thereof, for $Re \leqslant 3000$ and $0.002 \leqslant h \leqslant 0.9$, and checked all cases where $-0.005 < \omega_{i0} < 0.005$. The spatial growth rate (α_i) for the classical spatial stability analysis (where α_i is obtained for real ω) was then obtained by plotting the $\omega_i = 0$ contour in the complex α plane. We have verified that the system remains temporally unstable even for very low interface heights (including down to $h = 0.002$) in the range of Re investigated here.

Figure 2 shows the effect of Re on the spatial growth rates. It is seen that $\omega_i = 0$ occurs on several 'spatial' branches. The spatial branch from $\alpha_i = 0$ is henceforth denoted by α^*; the other branches are denoted as indicated in the figure. The coalescence of branches in the lower half of the complex α plane into a saddle point indicates the transition from convective to absolute instabilities. This is found to occur in the present case at $Re = 55$; the saddle-point method coupled with the cusp-map technique does not show any evidence of a pinched saddle node in this case for

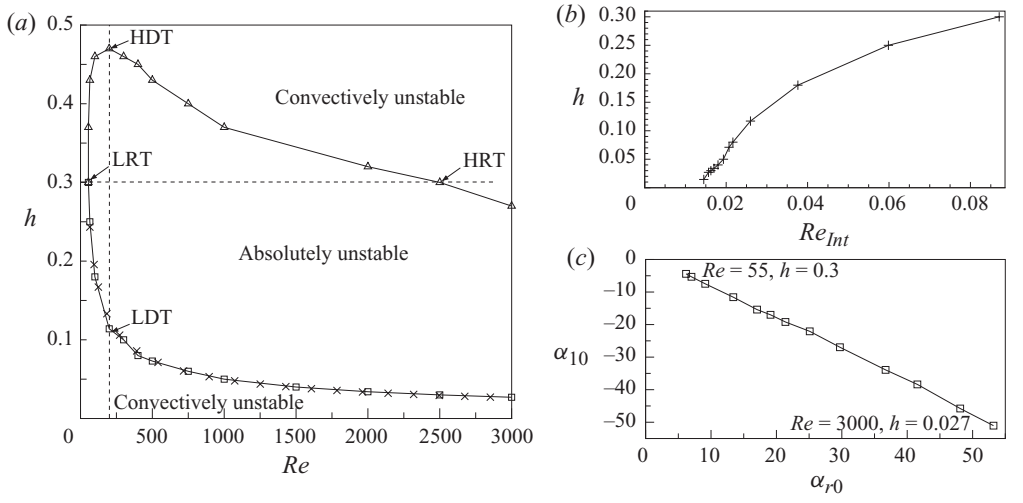

FIGURE 3. Regime transitions: (*a*) the loci of all the transition points, the stability map. A transition is identified as a point where $\omega_{i0} = 0$. (△), HD transition points; (□), LD transition points; (×), LDT points fitted to the power law $h = 1.6Re^{-0.5}$. (*b*) Variation of the lower-branch C/A transition $h = h_c$ with interfacial Reynolds number Re_{int}, and (*c*) LD transition points plotted on α space. Parameter values are $m = 30$, $\Gamma = 0.01$ and $r = 1$.

any $Re < 55$, indicating that the interfacial behaviour is convectively unstable in this region.

We have determined the boundary between convective and absolute instability by first plotting contours of ω_i on the complex α plane, and by subsequently determining the value at the saddle point ω_{i0}. For most cases studied here, only one saddle point could be identified for flows that were found to be absolutely unstable. However, for relatively thin films ($h \leqslant 0.04$) at high flow rates ($Re \geqslant 750$) or for large values of Γ, multiple saddle points were obtained, but only one pinched. These cases are discussed further below.

We have determined the transition points between convective and absolute instability (C/A) for a range of flow parameters. As explained in the Introduction, a full parametric study is not the subject of this paper; qualitatively, the trends are similar to those reported in Sahu *et al.* (2009) for miscible three-layer systems. In summary, for systems with a density contrast the flow is usually convectively unstable (hence air–water and air–oil systems were found to be convectively unstable for the range of Re studied); the same is found even for density-matched cases if the viscosity contrast is sufficiently close to unity, and for a large range of values of Γ (we return to this last point at the end of this section however). In the remaining cases, the flow is found to be absolutely unstable at an intermediate range of Re and h values, which we investigate in more detail here, as this is beyond the range of parameters that could be studied with the numerical method of Sahu *et al.* (2009).

Transitions C/A are shown for a range of cases in a $h - Re$ plot in figure 3(*a*). The region bounded within the curve corresponds to a parameter set for which absolute instabilities occur. The transitions at low and high Re are henceforth referred to as 'LRT' and 'HRT', respectively, and those at low and high h by 'LDT' and 'HDT', respectively. At the LDT, for $Re > 750$, two saddle points were found of which only one pinched.

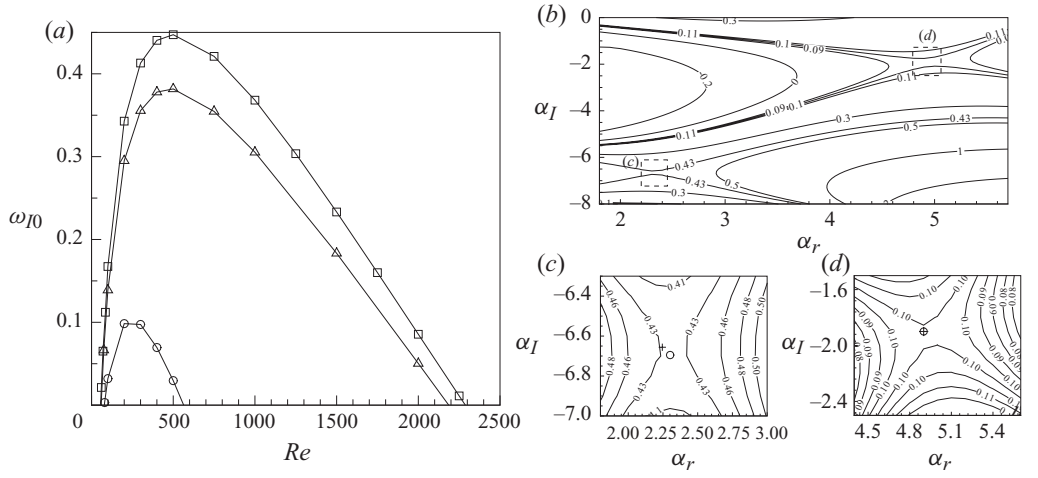

FIGURE 4. Effect of dimensionless surface tension, Γ. (a) Absolute growth rate ω_{i0} versus Reynolds number Re for different values of Γ: (□), $\Gamma = 0.01$; (△), $\Gamma = 1$; (○), $\Gamma = 10$. Other parameter values are $m = 30$, $r = 1$, $G = 0$. (b) Contours of ω_{i0} in the complex α plane for $Re = 200$, $\Gamma = 10$ with all other parameters as in (a) show two saddle points. These poles are enlarged in (c) and (d). The circles indicate the saddle point and the pluses indicate cusps; these match only for the right-hand pole indicating it as a pinching saddle point. The left-hand pole is non-pinching.

Of particular interest is the LDT: for relatively thin films, there is a critical height beyond which the system is absolutely unstable, and this extends over a large range of Re values. At this point it is important to remember that Re is based on the total flow rate through the entire channel, of both fluids. The results for the LDT can be seen as evidence for a critical value of a Reynolds number based on the height and properties of the thin film and the dimensional interfacial velocity of the base state (U_{int}), $Re_{int} \equiv \rho_B h U_{int}/\mu_B = (r/m)h(U_{int}H/Q)Re$, as follows. If we approximate the velocity in the film by simple shear, then a constant critical value of $Re_{int} = Re^c_{int}$ corresponds to a critical height $h_c \sim (mRe^c_{int}/rRe)^{1/2}$. Hence, $h_c \sim 1/\sqrt{Re}$. The results for the LDT shown in figure 3(a) are seen to accurately follow this prediction. In figure 3(b), it is seen that the value of Re_{int} approaches a constant as h_c is lowered: the points corresponding to the lowest values of h_c in figure 3(b) correspond to $Re = 2500$, 3000 and 10 000.

The results show, however, that a long-wave approximation would not be appropriate in this case. This can be seen as follows. Figure 3(c) depicts the trajectory of the LDT points in the α space. Evidently, at higher Re the saddle point corresponds to shorter waves with larger spatial growth rates, even at lower interface heights. The results shown can be approximated by a straight line, $\alpha_{i0} \approx 1.7 - \alpha_{r0}$. So the spatial amplification of disturbance is evidently very high; the amplitude of the saddle-point wave would more than double over a single wave length.

These results are found to be relatively independent of the dimensionless surface tension coefficient, Γ up to $\Gamma = 1$. For larger surface-tension values, however, the absolute growth rate has significantly dropped. In figure 4(a), the value of ω_{i0} is shown as a function of Re for different values of Γ at a fixed interface height h. However, for $\Gamma = 10$ two saddle points were obtained, of which only one pinched as shown in figure 4(b) for $Re = 200$. We have verified that the small deviation between the locations of the cusp and the saddle points in the cases of non-pinching saddle

points is independent of the number of collocation points used for solving the full Orr–Sommerfeld problem. Finally, we have checked that the most dangerous temporal mode for $\Gamma = 10$ is still an interfacial mode.

4. Numerical simulations of linear and nonlinear behaviour

In this section, the results of numerical simulations are discussed in detail following a brief description of the numerical procedure used to carry out the computations. Connections with the linear theory predictions presented in § 3 are made where appropriate.

4.1. *Numerical method*

One of the objectives of the present work is to study the wave evolution in the nonlinear regime using full numerical simulations. The diffuse-interface method of Ding *et al.* (2007) is used here (which closely follows Jacqmin 2000). Thus the volume fraction of the lower fluid, c, is used as the order parameter such that $c = 0$ and $c = 1$ correspond to the bulk of the upper and lower fluid, respectively. In this method, the volume fraction is governed by the advective Cahn–Hilliard equation, which in dimensionless form is given by

$$\frac{\partial c}{\partial t} + \boldsymbol{u} \cdot \nabla c = \frac{1}{Pe} \nabla \cdot (M \nabla \phi), \tag{4.1}$$

where the mobility M depends on volume fraction as $M(c) = c(1 - c)$; $\phi = 6\sqrt{2}\gamma(\varepsilon^{-1}\Psi'(c) - \varepsilon \Delta c)$ is the chemical potential, $\Psi(c) = c^2(1-c)^2/4$ is the bulk energy density that has minima at $c = 0$ and 1 (corresponding to the two bulk fluids), γ is the interfacial tension, ε is a measure of the thickness of the diffuse interface and $Pe = HU/(M_0\phi_0)$ is the Peclet number; here, M_0 and ϕ_0 are the characteristic values of mobility and chemical potential. As in Ding *et al.* (2007), we use $Pe = 1/\varepsilon^2$; the value of ε is limited by the grid spacing, and is set to $\varepsilon = 0.5\Delta x$, which corresponds to a thickness of the interfacial region (in terms of the distance between contours of $c = 0.1$ and 0.9) of around $3\Delta x$. The diffusion term in (4.1) originates from thermodynamics, and provides a mechanism to maintain the regularity of the interface. The Cahn–Hilliard equation is solved simultaneously with the following equations of continuity and momentum:

$$\nabla \cdot \boldsymbol{u} = 0, \tag{4.2}$$

$$Re\ \rho \left[\frac{\partial \boldsymbol{u}}{\partial t} + \boldsymbol{u} \cdot \nabla \boldsymbol{u} \right] = -\nabla p + \nabla \cdot [\mu(\nabla \boldsymbol{u} + \nabla \boldsymbol{u}^T)] + \Gamma \phi \nabla c - G \boldsymbol{e}_y. \tag{4.3}$$

The dimensionless values of the local viscosity and density are calculated using the local volume fractions of the respective layers, i.e. $\rho = (1 - c) + c\ r$, $\mu = (1 - c) + c\ m$. The choice of the smoothing function may affect the dynamics of small waves on the interface for coarse grids. Coward *et al.* (1997) argued that shear rate rather than viscosity should be smoothed for simulation of flows in which interfacial shear is dominant. Such a method results in a harmonic smoothing of viscosity across the interface. We have found this argument to be of benefit in our earlier work (Valluri *et al.* 2008), wherein a level-set method was used, resulting in a substantial reduction of discretization errors, yielding better agreement between our numerical and theoretical predictions of the linear growth rate for a given grid. In the present work based on the diffuse-interface method, however, harmonic smoothing was found to require a finer grid to get comparable results when comparing to linear theory to those obtained

with the arithmetic smoothing that is used here. A standard projection finite-volume method is used herein on a MAC grid to solve the momentum equations, with Adams–Bashforth and Crank–Nicholson techniques for the advective and viscous terms, respectively. A split semi-implicit discretization is used for the Cahn–Hilliard equation. The advection term in the Cahn–Hilliard equation is discretized using a fifth-order weighted essentially non-oscillatory (WENO) scheme. Further details and results of convergence tests can be found in Ding *et al.* (2007), other applications of the same method with comparisons to other, independent work can be found in Ding & Spelt (2008).

Two types of simulations are reported in this study. In the first, we impose periodic boundary conditions at the ends of the domain, with a fixed pressure drop (hence the total flow rate through the domain may change in time). In the second type, inlet and outlet conditions were imposed on the left and right boundary of the domain, respectively. At the inlet, the velocity field is prescribed as discussed further below. Neumann conditions are used at the outlet, that is, zero normal gradient of velocity and volume fraction under a fixed pressure drop. Domain length to height ratios of up to 1:10 have been used, a ratio dictated by computational feasibility. The governing equations were solved on a MAC grid for the rectangular domain shown in figure 1, using square grid cells. The simulations were conducted using OPENMP on 8-processor machines.

The initial wave amplitude, measured by the interface displacement, is taken to be much smaller than the grid spacing. This is because the stability analysis described in § 3 is valid only for perturbations of infinitesimally small amplitude. If the initial amplitude is not very small, the pressure disturbance is too large for the linear analysis to be valid. We typically use an initial wave amplitude of $O(10^{-3})$. A complication arising from starting waves with such small amplitudes is that the approach to breakup of slender filaments requires many time steps. In some simulations, discretization errors around the interface, related to the discretization of the surface-tension term, accumulate over these rather long integration times, when the wave amplitude is much smaller than the grid spacing. These discretization errors may give rise to disturbances generating spurious currents, though small in magnitude (cf. Lafaurie *et al.* 1994), unless large values of Γ are simulated. In this paper, we focus on modest values of Γ, which still allows us to study the C/A transition.

4.2. *Spatially periodic simulations*

We briefly investigate spatially periodic flows here, primarily with the objective to report on convergence studies, and comparisons with previous work. Also, ligament formation is observed in these simulations, which also feature in the results presented in the subsequent sections; the small domain used in the present section allows this process to be well resolved for relatively long times.

For these purposes, we report here on the evolution of a sinusoidal wave that corresponds approximately to the most-dangerous temporal mode for $h = 0.3$, $m = 30$, $r = 1$, $\Gamma = 0.01$, $G = 0$ and $Re = 50$, which is approximately $\alpha = 2\pi$ (hence we use a square domain here). Cases similar to this are simulated for open-ended channels in the next section, and it is seen in the previous section that such flow parameters are close to a C/A transition.

Figure 5 shows the effect of grid spacing on a semilog plot of the disturbance amplitude a versus time; a is obtained by subtracting the undisturbed base state interfacial depth from the instantaneous maximum interface height in the domain. The growth rates correspond to the slopes of the curves in figure 5(a). In table 1, the

Grid	ω_i	$c_r = \omega_r/\alpha_r$
120×120	0.30	0.18
240×240	0.33	0.18
480×480	0.34	0.19
Theoretical	0.34	0.21

TABLE 1. Dependence of the growth rate and wave speed on mesh spacing for temporally unstable flows. Parameters used are $L = 1$, $h = 0.3$, $m = 30$, $r = 1$, $\Gamma = 0.01$, $G = 0$ and $Re = 50$. The CFL number was kept constant between different grids.

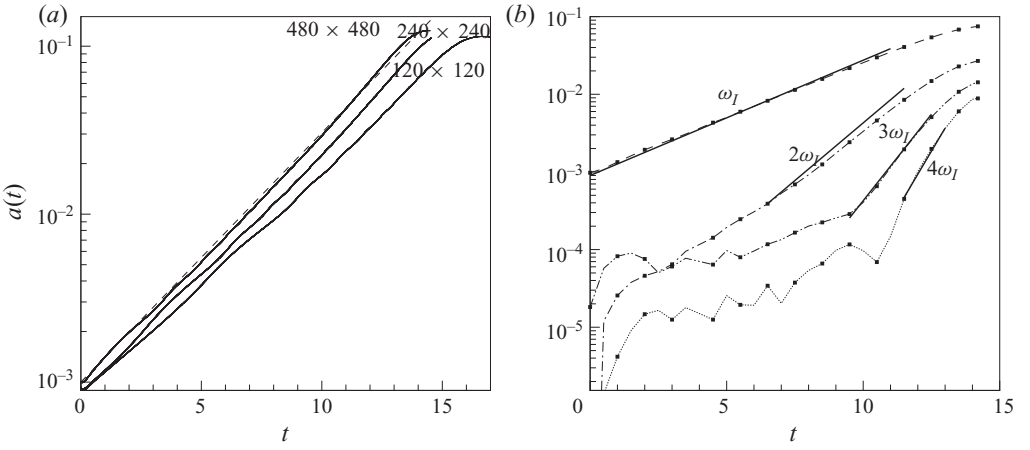

FIGURE 5. (*a*) Convergence study. Maximum perturbation height as a function of time for the most unstable mode. Solid and dashed lines represent the numerical simulation (for the grids indicated) and linear stability analysis, respectively. (*b*) Time evolution of amplitude of the fundamental mode and overtones. In both figures, $h = 0.3$, $m = 30$, $r = 1$, $\Gamma = 0.01$, $G = 0$ and $Re = 50$.

growth rate and the wave speed obtained from the simulations are compared with those obtained from the temporal linear stability theory. It was also verified that the Fourier transform of the wave evolved with the same growth rate as the maximum interface height. The growth rates from the numerical simulations appear to converge rapidly to those predicted from linear theory upon mesh refinement; the wave speed does approach the theoretical value but a very fine grid would be required to possibly achieve very close agreement. Additional tests (not shown) with even smaller initial amplitudes, as low as $O(10^{-6})$, gave results very close to those reported here. In figure 6 it can be seen that the velocity field also closely matches the linear theory (we have verified that throughout the linear stage the DNS curve shown in this figure does not change visibly). We therefore conclude that the degree of agreement with linear theory, and the general trends seen when refining the grid, are similar to that found in our previous work wherein a level-set method was used (Valluri *et al.* 2008).

From figure 5(*a*) we see that after around $t = 12$ for the finest grid used, there is a substantial departure from the linear (i.e. exponential) growth regime. To illustrate this more clearly, we show in figure 5(*b*) the growth of the first four Fourier modes of the interface profile, which has an initial dimensionless amplitude of 10^{-3}. The results show that once the overtones are expected to be more or less resolved, their growth rate briefly (and only approximately) satisfy the relation $\omega_i^k = (k+1)\omega_i$, where

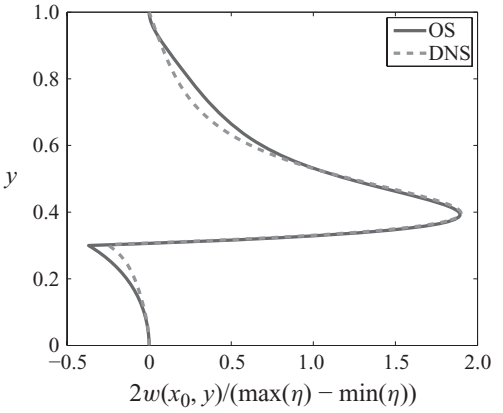

FIGURE 6. Comparison between linear theory (solid line) and DNS (dashed line) of the vertical velocity component w as a function of y across the wave crest (at $x = x_0$). The velocity has been scaled with the wave amplitude. Flow conditions as in figure 5 at $t = 3$ with $Ny = 480$. OS = Orr–Sommerfeld, DNS = direct numerical simulation.

k is the overtone number, and ω_i is the growth rate of the fundamental mode. This would suggest that the overtones are enslaved to the fundamental mode at this early stage (cf. Barthelet, Charru & Fabre 1995). This seems reasonable, even though the system studied here is far from criticality (the first four overtones shown here are all unstable themselves): the fundamental mode was imposed at $t = 0$ and may be expected to initially drive the growth of overtones. A comparison with fully weakly nonlinear theory is not the aim of this section.

The late-time wave evolution is summarized in figure 7(a–d). After nonlinear distortion, a ligament is seen to be formed. This is not observed for relatively large values of h, for which we have investigated in detail the nonlinear distortion in our previous work (Valluri *et al.* 2008). In figure 7(b) it is seen that this ligament is stretched by the surrounding flow, consistent with the findings of Boeck *et al.* (2007). This involves normal stresses inside the ligament that lower the pressure inside the ligament, thereby creating a sharp pressure gradient at the root of the ligament (see figure 7c), which drives fluid from the lower layer to enter the ligament. Meanwhile, the height of the wave at the root of the ligament only slowly increases during this stage (as can be verified by comparing this height in figures 7c and 7d). The streamwise locations of the root and tip of the ligament are traced in time in figure 8 for modest and relatively large values of Re. It is of interest to note a sudden acceleration of the streamwise location of the ligament tip, especially at low Re, obviously leading to an acceleration in the rate of stretching of the ligament. We have verified that the acceleration occurs at the point whereat the ligament tip has reached the trough of the periodic wave. The acceleration is therefore due to advection and stretching by the flow past the crest downstream of the original wave crest. Hence we conclude that interaction with downstream waves can have a significant effect on the rate of stretching of a ligament. Finally, we note in figure 8(a) that once the ligament has stretched to the point that the ligament thickness becomes comparable to the interfacial thickness, the ligament defined by the $c = 0.5$ contour breaks, but the subsequent trend in the figure is seen to be consistent with those at earlier times. In the Cahn–Hilliard formulation, the $c = 0.5$ contour does not break due to numerical error, but due to the minimization of the local free energy.

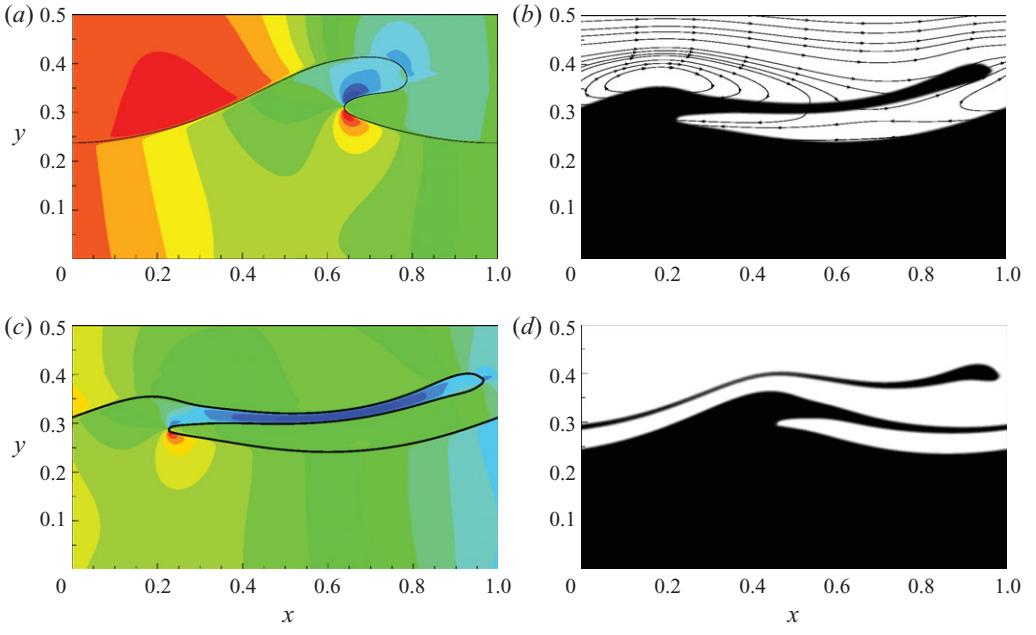

FIGURE 7. Temporal wave evolution for $Re = 50$, $Ny = 480$ (only the lower half of the domain is shown) for $t = 16.6$ (*a*), $t = 20$ (*b*, *c*) and $t = 21.4$ (*d*). In (*a*) and (*c*), the contours represent the pressure distribution. The instantaneous streamlines shown in (*b*) are in a frame of reference moving with the horizontal velocity component of a point on the ligament.

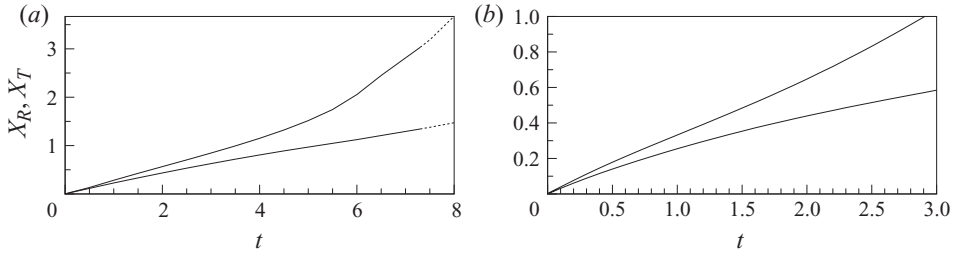

FIGURE 8. Ligament dynamics: the streamwise location of the ligament tip X_T and root X_R versus time from the onset of overturning for $Re = 50$ (*a*) and $Re = 500$ (*b*) with $Ny = 480$. Other parameter values are $h = 0.3$, $m = 30$, $r = 1$, $\Gamma = 0.01$, $G = 0$.

Tests showed the periodic domain to be prohibitive when investigating the convective/absolute nature of instabilities, because disturbances originating from a test pulse in the middle of the domain reach their periodic images too quickly. We therefore use in- and outlet conditions in the subsequent sections.

4.3. *Simulations with a localized disturbance in open systems*

We study here the spatio-temporal evolution of instabilities in relatively long channels (of aspect ratio 1:10) by introducing a small-amplitude interfacial forcing localized in the central region of the channel for a short duration of time. This is done by employing a body force of the form, $F_{imp} = \beta \partial c/\partial z$, in the y-momentum equation. Here, $\beta = A(-1 + \cos(2\pi(x - 5.0)))$ for $4.5 \leqslant x \leqslant 5.5$ and $t \leqslant 0.006$, but equal to zero for all other values of x and t. The factor A is chosen such that the resulting initial

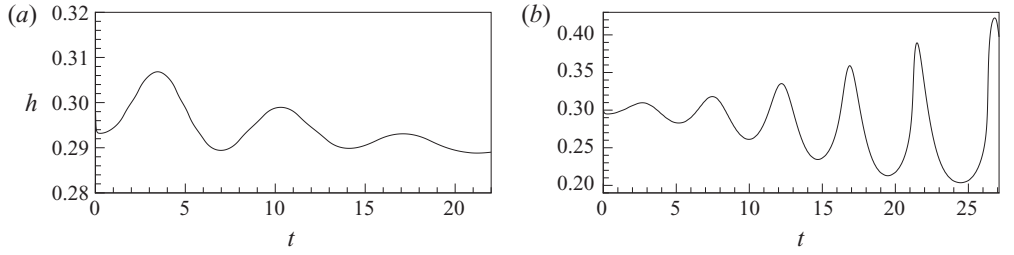

FIGURE 9. Evolution of the interfacial height at $x = 5$ following the introduction of a localized forcing around $x = 5$ as described in the main text (forcing switched off after $t > 0.006$) for $Re = 30$ (a) and 100 (b). Other parameters are: $H : L = 1 : 10$ at $(Nx \times Ny) \equiv (1800 \times 180)$; $h = 0.3$, $m = 30$, $r = 1$, $\Gamma = 0.01$ and $G = 0$.

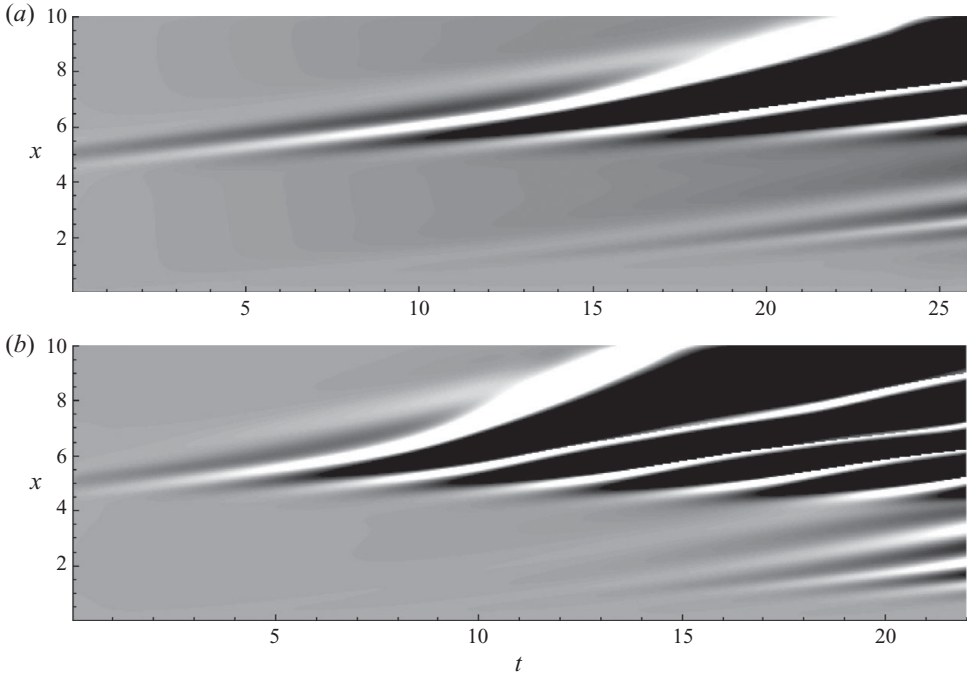

FIGURE 10. The (x, t) plots of the minimum interfacial height obtained following the introduction of a localized forcing around $x = 5$ as described in the main text (forcing switched off after $t > 0.006$) for $Re = 30$ (a) and 100 (b). Other parameters are $H : L = 1 : 10$ at $(Nx \times Ny) \equiv (1800 \times 180)$; $h = 0.3$, $m = 30$, $r = 1$, $\Gamma = 0.01$ and $G = 0$.

amplitude of the wave so generated is approximately 0.006 after the initial forcing, arguably small enough for linear theory to be valid (as suggested by figure 5).

In figures 9 and 10, results are shown for cases that are linearly convectively ($Re = 30$ with $A = 20$) and absolutely ($Re = 100$ with $A = 5$) unstable. In figure 9(a), it can be seen that the amplitude of the disturbance at the central point of the forcing ($x = 5$) decays for the convectively unstable case. In figure 10(a), the initial disturbance is seen to be convected downstream in this case. Conversely, the corresponding results for $Re = 100$ (a linearly absolutely unstable case) show evidence of sustained growth of disturbance at a frequency $\omega_r = 1.4 \pm 0.1$ at $x = 5$, which agrees quite well with the saddle mode frequency predicted by the linear theory ($= 1.61$). Close inspection of

figure 10(*b*) suggests there is evidence of propagation in the upstream direction, albeit at a rather slow rate. We conclude that these results are consistent with the findings of the linear spatio-temporal stability analysis.

It is seen in figure 10 that both simulations are overwhelmed quickly by disturbances convected from the inlet, as is to be expected from an unstable system. Small disturbances are generated at the inlet because the inlet profiles that are used as boundary conditions for velocity and volume fraction not necessarily exactly match with the discretized equations of motion. In preliminary simulations (not reproduced here), the analytical unidirectional parabolic two-layer velocity profile was used. This was found to yield even stronger wave growth from the inlet, because the analytical solution is not exactly equal to the solution of the velocity field that would be obtained numerically for a flat interface. In an effort to further reduce such disturbances, the present results have been obtained using a so-called numerical inlet profile (instead of the analytical profile), which was obtained from a simulation using periodic conditions for a very short domain (to ensure that the interface was kept flat) using the same number of grid spacing across the channel height, Ny. Given that an investigation of the long-time behaviour of these systems would require a very long computational domain indeed, we instead investigate the wave evolution and the comparison with linear theory in more detail in simulations with forcing at the inlet, in the next section.

4.4. *Simulations with random forcing at the inlet of open systems*

We study here the nonlinear spatio-temporal evolution of instabilities in relatively long channels by introducing small-amplitude random forcing to displace the interface at the inlet. In all the cases described here, constant flow rate conditions are imposed at the channel inlet; a Neumann-type outflow condition is applied at the outlet described by $\partial \boldsymbol{u}/\partial x = 0$ and $\partial c/\partial x = 0$. No-slip and no-penetration boundary conditions are imposed on the top and bottom channel walls. The initial conditions for the velocity correspond to the numerical base state, for reasons described in § 4.3.

We introduce random-phase noise in the system by changing the height at the inlet $h + A(t)$ according to (Chang *et al.* 1996)

$$A(t) = \int_0^\infty |\hat{A}(\omega_f)| \mathrm{e}^{\mathrm{i}(\omega_f t + \theta(\omega_f))}\, \mathrm{d}\omega_f, \tag{4.4}$$

where $\theta(\omega_f)$ is the phase of the complex amplitude $\hat{A}(\omega_f)$ and ω_f is a real perturbation frequency. On approximating (4.4) with N_f frequency units of width $\Delta\omega_f = \omega_{max}/N_f$, where ω_{max} is some high frequency cutoff we find

$$A(t) = \frac{A_0}{N_f} \sum_{k=0}^{N_f} \mathrm{e}^{\mathrm{i}(k\omega_{max} t/N_f + \theta_k)}. \tag{4.5}$$

The phase θ_k is a randomly generated phase angle between 0 and 2π and $A_0 = \hat{A}\omega_{max}$ is an arbitrarily specified amplitude such that $A(t) = O(10^{-3})$. We have chosen $N_f = 1000$ and $\omega_{max} = 3\omega_{max}^{\mathrm{T}}$, where $\omega_{max}^{\mathrm{T}}$ is the real frequency corresponding to the maximum temporal growth rate, such that a wide range of frequency spectrum is accounted for. Chang *et al.* (1996) chose the maximum cutoff frequency as twice the frequency of the neutral mode.

We have also conducted tests to establish the sensitivity of the results in this section to the grid spacing. As in the previous section, we use $Ny = 180$. Results obtained with $Ny = 90$ (and even $Ny = 60$) were found to be qualitatively very similar to those

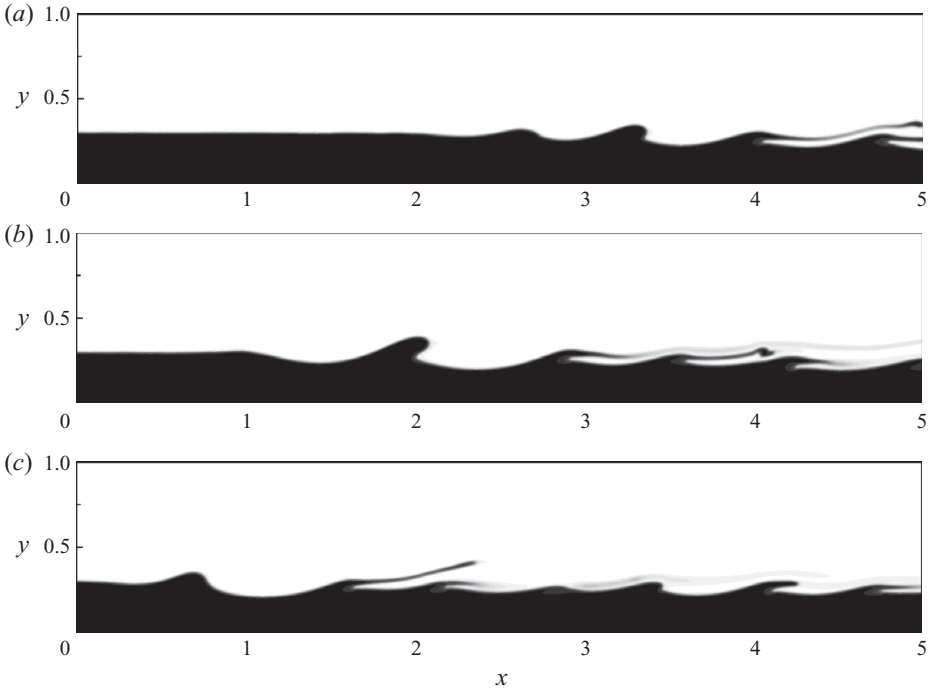

FIGURE 11. Snapshots of interface profiles from simulations with random forcing at the inlet, for various values of Re ($Re = 30$ (a), 55 (b), 100 (c). Other parameters are $h = 0.3$, $m = 30$, $r = 1$, $\Gamma = 0.01$, $G = 0$, $Re = 50$ for the analytical inlet profile.

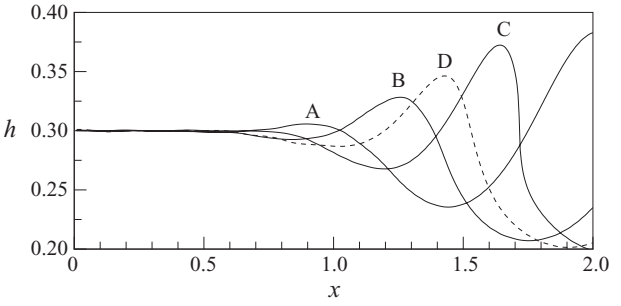

FIGURE 12. Successive wave profiles: curves A, B and C are for successive times at intervals of two time units; curve D is for 4.5 time units later than curve C. Parameter values used are $h = 0.3$, $m = 30$, $r = 1$, $\Gamma = 0.01$, $G = 0$ and $Re = 55$ for the numerical inlet profile.

reported here; the only difference is that the phenomena observed occur further downstream when using a coarse grid.

In figure 11, snapshots are shown of typical interface profiles. Motivated by the C/A transitions found from the linear analysis, we focus here mainly on the effect of the value of Re on the results for $r = 1$, $m = 30$, $h = 0.3$, $\Gamma = 0.01$ and $G = 0$. In figure 12, the typical evolution near the inlet is shown. In all the simulations, the sequence A–D shown in figure 12 is repeated continuously, after an initial transient, leading to an initially almost regular wavetrain.

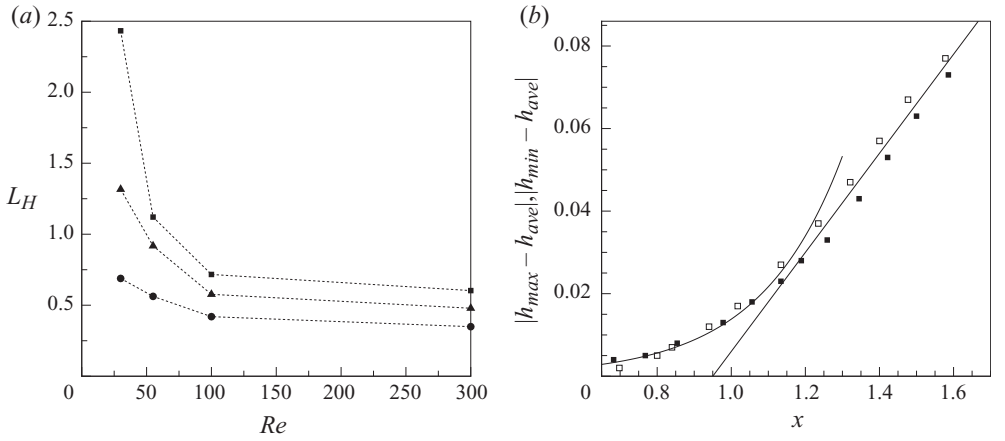

FIGURE 13. Healing length versus Re for different threshold values (a) and the time-averaged maximum and minimum interface height (b) for $Re = 55$. In (a), results are shown for threshold levels corresponding to 1 %, 5 % and 10 % of the base height of the interface h. In (b), the open symbols correspond to $|h_{max} - h_{ave}|$, the filled symbols to $|h_{min} - h_{ave}|$, where $h_{ave} = 0.297$; the slope of the straight line is 0.12, and the curved line is an exponential curve with exponent 4.5, corresponding to the spatial saddle point growth rate α_{i0}. The numerical inlet profile was used here.

The spatial growth rate observed in figure 12 does seem rather large. We compare here the case of $Re = 55$ with linear theory, as this corresponds to the C/A boundary, i.e. where $\omega_{i0} = 0$, which simplifies a comparison with the numerical simulations: because the variance of forcing is constant, there is no temporal growth at the inlet, but there would be for disturbances that have been transported further downstream in cases away from the C/A boundary. To facilitate a comparison with linear theory, we have determined from contour plots of the height $h(x, t)$ in the (x, t) plane the averaged distance where for the first time the interface reaches a height h_{max} for a range of values of h_{max}. We have repeated this process for a minimum height h_{min}. The results are shown in figure 13(b). Here we have subtracted an averaged value such that both curves more or less overlap (this value changes somewhat for different values of x, as is discussed further below; the value used in the figure gives the best coincidence of the h_{max} and h_{min} graphs for the case shown). Two regimes can be identified: an initial, approximately exponential regime, and a later, approximately linear regime.

An exponential curve has been superimposed in the figure, the exponent corresponds to the value of $-\alpha_{i0}$ for the case under investigation. It is seen that these numerical simulation results for the early spatial development can be represented well with the linear theory corresponding to the spatial growth rate of the saddle node linear mode. We have also investigated cases away from the C/A transition. At $Re = 100$, for example, the results from the numerical simulations are qualitatively very similar to those shown in figure 13(b), but the exponent is then higher than $-\alpha_{i0}$ from linear theory. This would be expected, since here $\omega_{i0} > 0$ here and further amplifies the wave growth.

The spatial growth further downstream is seen in figure 13(b) to be governed by an approximately linear regime. We have verified that in the cases studied here, there is no significant dependency of the prefactor in this linear growth on the value of Re.

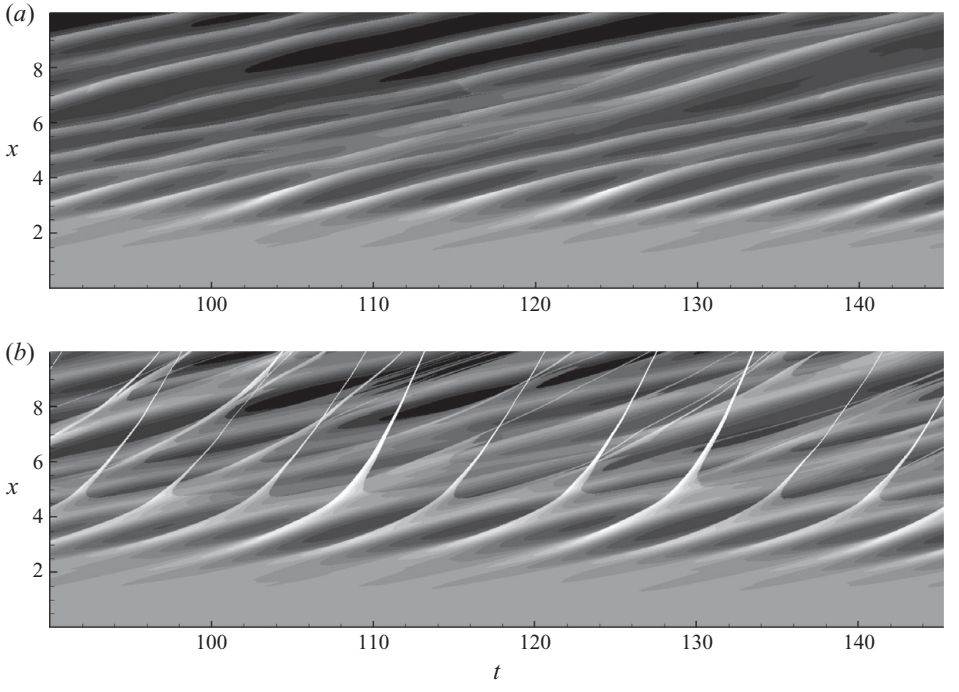

FIGURE 14. Space–time plot for $Re = 30$ with $H : L = 1 : 10$ at $(Nx \times Ny) \equiv (1800 \times 180)$ coloured by minimum interface height (a) and maximum interface height (b). The other parameters used are $h = 0.3$, $m = 30$, $r = 1$, $\Gamma = 0.01$ and $G = 0$.

A main effect seen in figure 11 is the increased spatial amplification of disturbances at larger Re. This is investigated further in figure 13(a), where we show the so-called 'healing length' as a function of Re. The healing length L_H is defined here as the distance from the inlet at which a prescribed interface elevation has been reached, and this value has been averaged over time. Results are shown for different threshold values. It was found that coarser grids showed the same trends, with a shift to somewhat larger for L_H. The results for sufficiently large threshold values show a fairly rapid decrease in the value of H when Re is increased beyond about $Re = 50$, after which it levels off. It is of interest to note that the C/A transition predicted by linear theory is at $Re = 55$ in this case (see figure 3).

The behaviour further downstream is investigated in figures 14 and 15, where results are shown for the elevation of the interface in (x, t) plots for different values of Re. The interface height here corresponds to the y-coordinate where $c = 0.5$. At any time t, more than one interface may be located at a streamwise location x (due to ligament formation), so the minimum as well as the maximum of the interface elevation is shown, the latter corresponding to the interfacial height of the ligament.

Once ligaments have reached a thickness that is comparable to the grid spacing, the $c = 0.5$ contours will eventually give the appearance of entrainment of droplets. Although the results presented here are for a relatively fine grid, such artificial entrainment events are observed in figures 14(b) and 15(b). The white streaks in these figures do not correspond to actual droplets, but merely to that part of ligaments wherein the value of c is still above 0.5. The results for periodic domains studied in § 4.2 suggest that this does not appear to affect the ligament dynamics (see figure 8a),

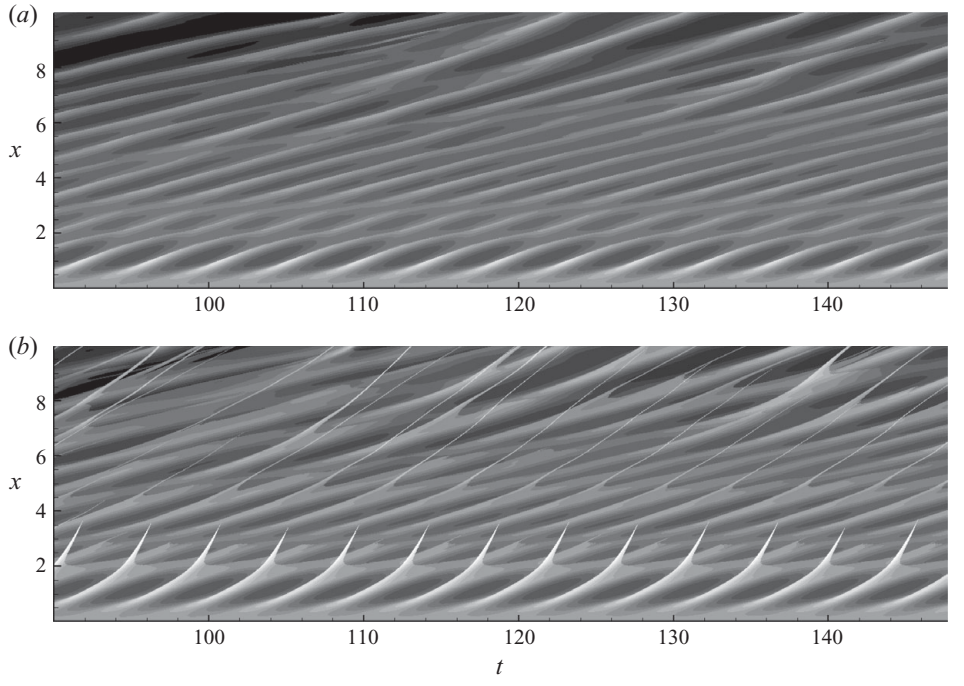

FIGURE 15. Space–time plot for $Re = 100$ with $H : L = 1 : 10$ at $(Nx \times Ny) \equiv (1800 \times 180)$ coloured by minimum interface height (a) and maximum interface height (b). The other parameters used are $h = 0.3$, $m = 30$, $r = 1$, $\Gamma = 0.01$ and $G = 0$.

as this is primarily in a regime wherein the ligament is almost passively advected. Also, we have verified that the results for coarser grids are qualitatively similar, the same phenomena occur but further downstream.

In figure 14, which is for $Re = 30$, it can be seen that four wave crests tend to coalesce into two. This coalescence mechanism appears to be robust, as it occurs on two occasions in a similar manner. Comparison with figure 14(b) shows that wave coalescence coincides with the rapid elongation of a ligament stemming from the upstream wave crest. A clear example (albeit for a different Re) is clearly visible in figure 11(c). But most ligaments are formed directly from uniformly growing waves, without coalescence phenomena.

Further evidence was obtained by taking Fourier spectra of the (x, t) graphs to determine the dominant values of ω_r. The spectra for $Re = 30$ and $Re = 100$ are shown in figure 16. It can be seen in figure 16(d) that in the absolutely unstable regime ($Re = 100$), at a short distance from the inlet ($x = 1$) where linear wave growth occurs, a single dominant frequency of 1.4 ± 0.1, which is the same as that observed in the pulse simulations in § 4.3, agreeing quite well with the saddle mode frequency predicted by the linear theory ($= 1.61$). In the convective regime the numerical simulation at $Re = 30$ shows no such distinct single dominant frequency (figure 16a). In both simulations a shift to lower frequencies is observed downstream in figures 16(b, c) and 16(e, f), consistent with coalescence phenomena observed in the corresponding (x, t) plots.

Also, the slopes of the streaks in the (x, t) plots were measured within a short distance from the inlet (where the waves are still small and there is exponential growth) and averaged to determine a wave speed c_r. Here, it was noted that the

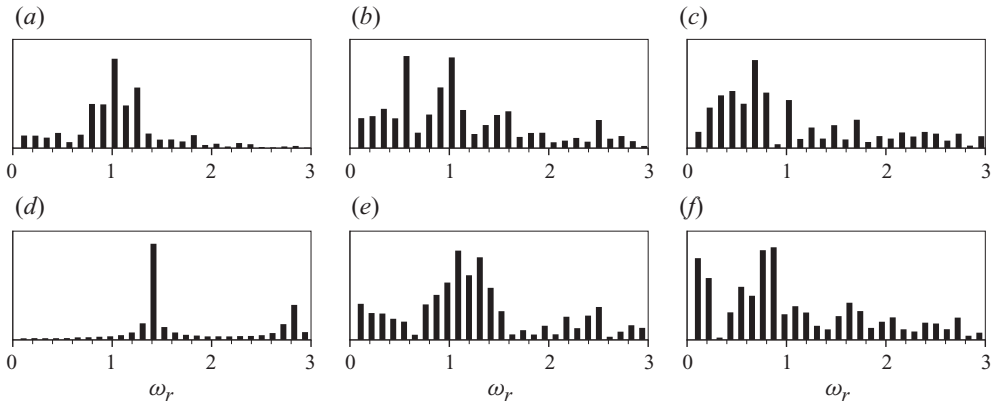

FIGURE 16. Fourier frequency strengths at the inlet (a, d), middle (b, e) and outlet (c, f) of the channel for $Re = 30$ (a–c) and $Re = 100$ (d–f) ($x = 2$, 4, 9.9, 1, 7, 9.9 in (a), (b), (c), (d), (e), (f), respectively). Other parameter values as in figures 14 and 15.

simulations are in agreement with the linear theory only for the cases that are no longer purely convective; for $Re = 100$, the simulation resulted in a wave speed of 0.22, which agrees with the saddle mode value ($c_r = \omega_{r0}/\alpha_{r0}$) of 0.23. This indicates that a randomly forced absolutely unstable system naturally selects a mode corresponding to the saddle point in the linear regime, whereas no such preference is made for a convectively unstable system.

In figure 15, which is for $Re = 100$, 'first-generation' ligaments are seen to be formed with remarkable regularity. After a ligament has been formed, the speed of the root or crest of the wave is seen to decrease briefly, before again acceleration to lead up to subsequent ligaments. Wave coalescence is observed, quite similar to that for $Re = 30$ in figure 14, but further downstream.

5. Conclusions

The spatio-temporal behaviour of two-layer flows in a two-dimensional channel has been investigated using linear theory and DNSs. Theoretical results were obtained by solving an Orr–Sommerfeld type problem for a complex growth rate keeping the wavenumber complex. Numerical results are obtained using a diffuse-interface method.

In most systems studied here the linear theory predicts convective instability. We have verified that the streamfunction amplitude profiles and energy budgets indicate that instability arises due to an interfacial mode (in the parameter range studied here), pointing to a Yih-type mechanism for instability arising from the viscosity contrast (cf. Boomkamp & Miesen 1996). A limited region in parameter space is found to give rise to absolute instability, i.e. for near and perfectly density-matched (i.e. liquid/liquid) systems at moderate Reynolds number values and interfacial height, if there is a viscosity contrast. It is found that thin films are predominantly convectively unstable, but that there is a critical interfacial Reynolds number beyond which the instability is absolute.

The main focus of the present paper is the application of an interface-capturing (diffuse-interface) method (Ding *et al.* 2007), to compare with results from linear theory discussed above and to investigate the later nonlinear development. We have first reported here results for two-layer channel flow for relatively long channels

showing the evolution of a temporary and spatially localized forcing in the middle of the domain. These clearly confirm predictions of linear theory as to the convective and absolute nature of instability of these flows. However, very small disturbances from the inlet (arguably due to small discretization errors in the inlet velocity profile that are unavoidable rapidly overwhelm the behaviour of any localized pulses, and it would require a very large computational effort to simulate the long-time behaviour of localized pulses.

Given the significance of disturbances created at the inlet for system sizes within the reach of the present simulation method, and because we anticipate experimental conditions to result in introduction of such disturbances, we have studied the system further using random interfacial forcing at the inlet instead. Again, waves are seen to grow rapidly at most values of Re. The spatial growth rate inferred from the simulations for a case on the C/A boundary compares well with linear theory. Also, the so-called healing length is found to drop when increasing the Reynolds number Re around the C/A transition predicted by linear theory. Fourier spectra of the time signal of minimum interface height at various spatial locations show a dominant frequency close to the inlet, multiple competing frequency modes indicating incipience of wave coalescence events in the middle and finally a lower dominant frequency close to the outlet of the channel, corresponding to a high amplitude wave resulting from wave coalescence events before it. For cases on the (C/A) boundary and those in the absolute regime, the dominant wave frequency close to the inlet agrees well with that saddle mode frequency. Wave speeds obtained for cases on the C/A boundary and in the absolute regime also agreed with values predicted by linear theory. Thus, a randomly perturbed system preferentially selects modes pertaining to the saddle point (in the linear regime), when the conditions favour the instability to be absolute. Further downstream, the results for the cases studied here show how wave coalescence coincides with ligament formation from the upstream wave. This is observed in cases that are either linearly convectively or absolutely unstable.

The DNSs presented here are naturally limited in parameter space, and focus primarily on the C/A boundary in this study; a more extensive parametric study is beyond the scope of this paper. We note that numerical methods for interface tracking normally struggle with much larger values than the relatively low values of a dimensionless surface-tension coefficient considered in this paper, due to the formation of parasetic currents that can only be reduced by using a much finer grid than used here.

This paper reports results from the ZEAL project TP//ZEE/6/1/21191, which involves Alfa Laval, Cadbury Ltd., Ecolab Ltd., Newcastle University, Scottish & Newcastle Ltd., GEA Process Engineering Ltd., Unilever UK Central Resources Ltd., Imperial College London, GlaxoSmithKline, Bruker Optics Ltd. and the University of Birmingham. The project is co-funded by the Technology Strategy Board's Collaborative Research and Development programme.

Appendix

In this appendix, we describe the equations and the numerical method for the linear stability analysis undertaken in § 3. In the 'base state', the interface is flat ($\eta = 0$), the flow is steady and unidirectional, $v = 0$, $u = U(y)$, and the pressure is linear, $p = (\mathrm{d}P/\mathrm{d}L)x$, under a negative dimensionless pressure gradient, $\mathrm{d}P/\mathrm{d}L$. The

solution for laminar velocity profile is then

$$U_A = \frac{\mathrm{d}P}{\mathrm{d}L}\frac{y^2}{2} + C_1 y + C_2, \tag{A 1}$$

$$U_B = \frac{1}{2}\frac{m^{-1}}{(\mathrm{d}P/\mathrm{d}L)}\left(\frac{\mathrm{d}P}{\mathrm{d}L}y + C_3\right)^2 + C_4. \tag{A 2}$$

The pressure gradient, $\mathrm{d}P/\mathrm{d}L$, and the integration constants, C_1, C_2, C_3 and C_4, are obtained by solving the following equations simultaneously:

$$\frac{1}{2}\frac{m^{-1}}{(\mathrm{d}P/\mathrm{d}L)}\left[\left(\frac{\mathrm{d}P}{\mathrm{d}L}h + C_3\right)^2 - (C_3)^2\right] - \frac{1}{2}\frac{\mathrm{d}P}{\mathrm{d}L}(h^2-1) - C_1(h-1) = 0, \tag{A 3}$$

$$C_2 = -\frac{1}{2}\frac{\mathrm{d}P}{\mathrm{d}L} - C_1, \tag{A 4}$$

$$C_3 = C_1, \tag{A 5}$$

$$C_4 = \frac{1}{2}\frac{m^{-1}}{(\mathrm{d}P/\mathrm{d}L)}(C_1)^2 \text{ and} \tag{A 6}$$

$$\int_0^h U_B \mathrm{d}y + \int_h^1 U_A \mathrm{d}y = 1. \tag{A 7}$$

Equations (A 3) and (A 5) are obtained from the continuity of velocity and continuity of shear stress at the interface, respectively. Equations (A 4) and (A 6) are obtained by no-slip boundary conditions at the top and bottom walls, respectively. Equation (A 7) represents a condition of constant volumetric flow rate, $Q \equiv VH$.

Perturbation equations: As mentioned in § 3, we study the stability of the system by subjecting the base state to a small amplitude perturbation. Each flow variable is expressed as a sum of the base state and the perturbation:

$$\eta = \epsilon\tilde{\eta}\mathrm{e}^{\mathrm{i}(\alpha x - \omega t)},\ u = U(y) + \epsilon\psi_y(y)\mathrm{e}^{\mathrm{i}(\alpha x-\omega t)},\ v = -\epsilon\mathrm{i}\alpha\psi(y)\mathrm{e}^{\mathrm{i}(\alpha x-\omega t)},$$
$$p = \frac{\mathrm{d}P}{\mathrm{d}L}x + \epsilon\tilde{p}(y)\mathrm{e}^{\mathrm{i}(\alpha x-\omega t)}. \tag{A 8}$$

Here ϵ is an arbitrary small parameter, $\tilde{\eta}$ is the relative amplitude of the perturbation, ψ is the (y-dependence of the) streamfunction and $\tilde{p}$ is the corresponding (y-dependence of the) pressure.

Substituting (A 8) into the equations of motion and boundary conditions, and dropping terms that are nonlinear in the perturbed variables, we get the following system of governing equations:

$$\mathrm{i}\alpha Re\left[(\psi_A'' - \alpha^2\psi_A)(U_A - c) - \psi_A U_A''\right] = \left(\psi_A'''' - 2\alpha^2\psi_A'' + \alpha^4\psi_A\right), \tag{A 9a}$$

$$\mathrm{i}\alpha r Re\left[(\psi_B'' - \alpha^2\psi_B)(U_B - c) - \psi_B U_B''\right] = m\left(\psi_B'''' - 2\alpha^2\psi_B'' + \alpha^4\psi_B\right) \tag{A 9b}$$

and boundary conditions: no-slip and no-penetrating conditions at the walls:

$$\text{at } y = 0 : \psi_B = \psi_B' = 0, \tag{A 9c}$$

$$\text{at } y = 1 : \psi_A = \psi_A' = 0, \tag{A 9d}$$

continuity of velocity and of the tangential and normal stress components and the kinematic condition at the interface, $y = h$:

$$\psi_A = \psi_B, \tag{A 9e}$$

$$\tilde{\eta} = \psi_A/(c - U_A) = \psi_B/(c - U_B), \tag{A 9f}$$

$$\psi'_A - \psi'_B + \tilde{\eta}\left(U'_A - U'_B\right) = 0, \tag{A 9g}$$

$$\psi''_A + \alpha^2\psi_A - m\left(\psi''_B + \alpha^2\psi_B\right) = 0, \tag{A 9h}$$

$$\alpha r Re\left[\psi'_B(c - U_B) + \psi_B U'_B\right] - \alpha Re\left[\psi'_A(c - U_A) + \psi_A U'_A\right]$$
$$-m\left(\psi'''_B - 3\alpha^2\psi_B\right) + \left(\psi'''_A - 3\alpha^2\psi'_A\right) - (\Gamma\alpha^2 + G)\alpha\left(\frac{\psi'_B - \psi'_A}{U'_A - U'_B}\right) = 0. \tag{A 9i}$$

Equations (A 9*a*)–(A 9*i*) constitute an eigenvalue problem for the streamfunctions, ψ_A and ψ_B, with eigenvalue, $\lambda = -i\alpha c = -i\omega$ at a given Reynolds number. We have verified that this system is consistent with earlier work, (e.g. Boomkamp *et al.* 1997).

Numerical solution: We solve (A 9) using the Chebyshev collocation method described by Boomkamp *et al.* (1997), wherein a trial solution involving the Chebyshev polynomials $T_j(\cdot)$ is proposed in each domain:

$$\psi_A(y) = \sum_{j=0}^{N_A} a_j T_j(\eta_A), \qquad \psi_B(y) = \sum_{j=0}^{N_B} b_j T_j(\eta_B); \tag{A 10}$$

this reduces the differential equations (A 9) to a finite-dimensional eigenvalue problem. The variables η_A and η_B are linear transformations of the y-coordinate, such that $\eta_A, \eta_B \in [-1, 1]$. The trial solution ψ_A is substituted into the differential equation (A 9*a*) and evaluated at $N_A - 3$ interior points; the same thing is done for the trial solution ψ_B in (A 9*b*). This gives $N_A + N_B - 6$ equations in $N_A + N_B + 2$ unknowns; the system is closed by evaluating the trial functions at the boundaries $y = 0$ and $y = 1$, and at the interface $y = h$. In this way, a finite-dimensional analogue of (A 9) is obtained:

$$\boldsymbol{A}\psi = -\mathrm{i}\alpha c\boldsymbol{B}\psi, \tag{A 11}$$

where $\boldsymbol{A}$ and $\boldsymbol{B}$ are $(N_1 + N_2 + 2) \times (N_1 + N_2 + 2)$ complex matrices, and $\psi \in \mathbb{C}^{N_1+N_2+2}$ is a vector. The eigenvalue $\lambda = -\mathrm{i}\alpha c$ is obtained using a standard eigenvalue solver.

As in Trefethen (2000), we use the eigenvalue solver in MATLAB to solve (A 11). The advantages of using this technique over other numerical methods (e.g. in the work of Boomkamp *et al.* 1997) are twofold. First, the null rows in the matrix $\boldsymbol{B}$ (which correspond to infinite eigenvalues) do not affect the computation: we have performed calculations with these rows included or removed, and have verified that the value of the finite eigenvalues is the same in both cases. Second, the solver automatically balances the problem, which removes the possibility of ill-conditioning due to the large entries in $\boldsymbol{A}$ associated with high-order derivatives of Chebyshev polynomials. Thus, evaluation of the leading eigenvalue of (A 11) is rendered fast and accurate.

The approximation (A 10) converges exponentially in N_A and N_B to the solution of the differential equation pair (A 9*a*)–(A 9*b*). In the cases considered here, convergence has been achieved with $N_A = 51$ collocation points in the upper layer and from $N_B = 15$ (for $h \leqslant 0.05$) to a maximum of $N_B = 51$ (for $h = 0.5$) in the lower layer. The form of the trial solutions, wherein N_A and N_B are not necessarily equal, enables us to investigate thin bottom layers; previous work in this area (see Sahu *et al.* 2007, 2009)

involved a numerical method with $N_A = N_B$, which restricted the focus to relatively thick bottom layers.

REFERENCES

Barthelet, P., Charru, F. & Fabre, J. 1995 Experimental study of interfacial long waves in a two-layer shear-flow. *J. Fluid Mech.* **303**, 23–53.

Boeck, J., Li, J., López-Pagés, E., Yecko, P. & Zaleski, S. 2007 Ligament formation in sheared liquid/gas layers. *Theor. Comput. Fluid Dyn.* **21** (1), 59–76.

Boomkamp, P. A. M., Boersma, B. J., Miesen, R. H. M. & Beijnon, G. V. 1997 A Chebyshev collocation method for solving two-phase flow stability problems. *J. Comput. Phys.* **132** (2), 191–200.

Boomkamp, P. A. M. & Miesen, R. H. M. 1996 Classification of instabilities in parallel two-phase flow. *Intl J. Multiph. Flow* **22**, 67–88.

Chang, H.-C., Demekhin, E. A. & Kalaidin, E. 1996 Simulation of noise-driven wave dynamics on a falling film. *AIChE J.* **42** (6), 1553–1568.

Chomaz, J. M. 2005 Global instabilities in spatially developing flows: non-normality and nonlinearity. *Annu. Rev. Fluid Mech.* **37**, 357–392.

Coward, A. V., Renardy, Y. Y., Renardy, M. & Richards, J. R. 1997 Temporal evolution of periodic disturbances in two-layer Couette flow. *J. Comput. Phys.* **132**, 346–361.

Ding, H. & Spelt, P. D. M. 2008 Onset of motion of a three-dimensional droplet on a wall in shear flow at moderate Reynolds numbers. *J. Fluid Mech.* **599**, 341–362.

Ding, H., Spelt, P. D. M. & Shu, C. 2007 Diffuse interface model for incompressible two-phase flows with large density ratios. *J. Comput. Phys.* **226**, 2078–2095.

Duprat, C., Ruyer-Quil, C., Kalliadasis, S. & Giorgiutti-Dauphine, F. 2007 Absolute and convective instabilities of a viscous film flowing down a vertical fiber. *Phys. Rev. Lett.* **98**.

Fuster, D., Bague, A., Boeck, T., Le Moyne, L., Leboissetier, A., Popinet, S., Ray, P., Scardovelli, R. & Zaleski, S. 2009 Simulation of primary atomization with an octree adaptive mesh refinement and VOF method. *Intl J. Multiph. Flow* **35**, 550–565.

Huerre, P. & Monkewitz, P. A. 1990 Local and global instabilities in spatially developing flows. *Annu. Rev. Fluid Mech.* **22**, 473–537.

Jacqmin, D. 2000 Contact-line dynamics of a diffuse fluid interface. *J. Fluid Mech.* **402**, 57–88.

Lafaurie, B., Nardone, C., Scardovelli, R., Zaleski, S. & Zanetti, G. 1994 Modeling merging and fragmentation in multiphase flows with surfer. *J. Comput. Phys.* **113** (1), 134–147.

Lingwood, R. J. 1997 On the application of the Briggs' and steepest-descent methods to a boundary-layer flow. *Stud. Appl. Math.* **98**, 223–254.

Miesen, R. H. M. & Boersma, B. J. 1995 Hydrodynamic stability of a sheared liquid film. *J. Fluid Mech.* **301**, 175–202.

Sahu, K. C., Ding, H., Valluri, P. & Matar, O. K. 2009 Linear stability analysis and numerical simulation of miscible two-layer channel flow. *Phys. Fluids* **21**, 042104.

Sahu, K. C., Valluri, P., Spelt, P. D. M. & Matar, O. K. 2007 Linear instability of pressure-driven channel flow of a Newtonian and a Herschel–Bulkley fluid. *Phys. Fluids* **19**, 122101. (Erratum (2008), *Phys. Fluids* **20**, 109902.)

Schmid, P. J. & Henningson, D. S. 2000 *Stability and Transition in Shear Flows*. Springer.

Trefethen, L. N. 2000 *Spectral Methods in MATLAB*. SIAM.

Valluri, P., Spelt, P. D. M., Lawrence, C. J. & Hewitt, G. F. 2008 Numerical simulation of the onset of slug initiation in laminar horizontal channel flow. *Intl J. Multiph. Flow* **34** (2), 206–225.

Yecko, P., Zaleski, S. & Fullana, J.-M. 2002 Viscous modes in two-phase mixing layers. *Phys. Fluids* **14**, 4115–4122.

Yiantsios, S. G. & Higgins, B. G. 1988 Linear-stability of plane Poiseuille flow of two superposed fluids. *Phys. Fluids* **31** (11), 3225–3238.

Yih, C.-S. 1967 Instability due to viscosity stratification. *J. Fluid Mech.* **27** (02), 337–352.